

# Unsupervised Hyperspectral Mixed Noise Removal Via Spatial-Spectral Constrained Deep Image Prior

Yi-Si Luo, Xi-Le Zhao, Tai-Xiang Jiang\*, Yu-Bang Zheng, and Yi Chang

**Abstract**—Hyperspectral images (HSIs) are unavoidably corrupted by mixed noise which hinders the subsequent applications. Traditional methods exploit the structure of the HSI via optimization-based models for denoising, while their capacity is inferior to the convolutional neural network (CNN)-based methods, which supervisedly learn the noisy-to-denoised mapping from a large amount of data. However, as the clean-noisy pairs of hyperspectral data are always unavailable in many applications, it is eager to build an unsupervised HSI denoising method with high model capability. To remove the mixed noise in HSIs, we suggest the spatial-spectral constrained deep image prior (S2DIP), which simultaneously capitalize the high model representation ability brought by the CNN in an unsupervised manner and does not need any extra training data. Specifically, we employ the separable 3D convolution blocks to faithfully encode the HSI in the framework of DIP, and a spatial-spectral total variation (SSTV) term is tailored to explore the spatial-spectral smoothness of HSIs. Moreover, our method favorably addresses the semi-convergence behavior of prevailing unsupervised methods, e.g., DIP 2D, and DIP 3D. Extensive experiments demonstrate that the proposed method outperforms state-of-the-art optimization-based HSI denoising methods in terms of effectiveness and robustness.

**Index Terms**—Hyperspectral images, mixed noise removal, unsupervised learning, spatial-spectral constrained deep image prior, spatial-spectral total variation.

## I. INTRODUCTION

**H**YPERSPECTRAL images (HSIs) are images of the same scene captured by sensors across different wavelengths, which usually have hundreds of spectral bands. Compared with regular images, HSIs contain abundant spatial and spectral information and thus can be utilized into various applications, such as object detection [2], [3], classification [4]–[6], and so on. Due to the imaging environment, HSIs are inevitably corrupted by mixed noise, which includes, but not

\* Corresponding author.

This work is supported by the National Natural Science Foundation of China (61772003, 61876203) and the Fundamental Research Funds for the Central Universities (ZYGX2016J132, JBK2001011, and JBK2001035).

Y.-S. Luo, X.-L. Zhao, and Y.-B. Zheng are with the Research Center for Image and Vision Computing, School of Mathematical Sciences, University of Electronic Science and Technology of China, Chengdu, P.R.China (e-mail: yisiluo1221@foxmail.com; xlzhao122003@163.com; zhengyubang@163.com).

T.-X. Jiang is with the FinTech Innovation Center, the Financial Intelligence and Financial Engineering Research Key Laboratory of Sichuan province, School of Economic Information Engineering, Southwestern University of Finance and Economics, Chengdu, P.R.China (e-mail: taixiangjiang@gmail.com; jiangtx@swufe.edu.cn).

Y. Chang is with the Artificial Intelligence Research Center, Peng Cheng Laboratory, Shenzhen, P.R.China (e-mail: yichang@hust.edu.cn).

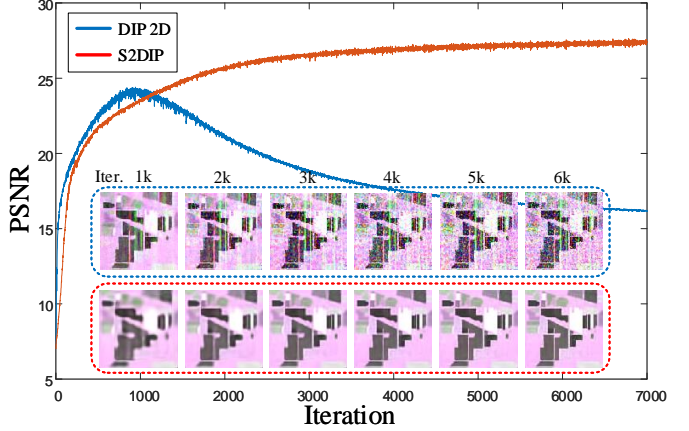


Fig. 1. The history of PSNR values of the denoising results by DIP 2D [1] and S2DIP with respect to the iterations. Compared to DIP 2D, S2DIP is more stable and achieves better results for HSI mixed noise removal.

limited to, Gaussian noise, impulse noise, deadlines, and stripe noise. The complex noise seriously affects the performance of the subsequent applications as well as visual qualities. Hence, HSI denoising is considered an essential technique in hyperspectral imaging.

Generally, the hyperspectral noise is modeled as

$$\mathcal{Y} = \mathcal{X} + \mathcal{V}, \quad (1)$$

where  $\mathcal{Y} \in \mathbb{R}^{H \times W \times B}$  denotes the observed data,  $\mathcal{X} \in \mathbb{R}^{H \times W \times B}$  denotes the underlying clean HSI, and  $\mathcal{V} \in \mathbb{R}^{H \times W \times B}$  is the mixed noise. The denoising technique is to estimate an ideal image  $\mathcal{X}$  from the observed data  $\mathcal{Y}$ . Earlier HSI denoising methods are dominated by model-based techniques, such as total variation (TV)-based methods [7]–[11], sparsity-driven methods [12], [13], and matrix/tensor low-rank-based methods [14]–[20]. These methods exploit the intrinsic structure of HSIs via optimization-based models to deal with the HSI denoising.

Inspired by the success of deep learning in inverse problems in imaging [21]–[26], the CNN-based methods for HSI denoising [27]–[32] have emerged in the last few years. Generally, most of the CNN-based methods learn the noisy-to-denoised mapping driven by abundant training data, e.g., Yuan *et al.* [30] employed the deep residual CNN to conduct HSI denoising. Dong *et al.* [28] utilized the deep 3D encoder-decoder network for HSI denoising.

Although great performance has been achieved by CNN-based methods, the effectiveness of them critically depends

on the diversity and quantity of the training data. However, the hyperspectral data is limited and the real noise of HSIs is complex. Thus, it is difficult to guarantee high-quality denoising results under the realist complex noise scenario of HSIs, where the underlying assumption is not held in the training data.

Recently, Ulyanov *et al.* proposed an unsupervised image restoration method, named deep image prior [33]. The DIP employs the CNN and optimizes its parameters by targeting the observed image as the network output with a randomly given input, demonstrating that the CNN itself can represent a well-reconstructed image by the iterative process without any training. Afterward, Sidorov *et al.* extended the DIP into HSI restoration, which yields promising performance on HSI denoising, inpainting, and super-resolution.

However, two issues are existing in the current DIP framework. Firstly, directly extending 2D convolution-driven DIP to 3D convolution-driven DIP is of limited benefits in the performance of HSI restoration [1]. Also, the 3D convolution brings abundant network parameters, leading to high computational burdens in the iterative process of DIP.

Secondly, the DIP suffers from the semi-convergence. The semi-convergence refers to the behavior of an iterative method that the PSNR value begins to increase at early iterations and, after a certain “optimal” iteration, the PSNR value begins to decrease, as seen in Fig. 1. Hence, the iteration needs to terminate by referring the ground-truth image at the point of the highest PSNR value, before fitting the noise.

Our purpose is to build an unsupervised HSI mixed noise removal method based on DIP, which simultaneously alleviates the aforementioned issues. Specifically, the separable 3D convolution blocks are utilized to faithfully extend the DIP for 3D HSIs. Meanwhile, a spatial-spectral total variation term is employed to explore the spatial-spectral local smoothness of HSIs and address the semi-convergence of DIP.

Compared to supervised CNN-based methods, the proposed method does not need any training data and is more applicable to handle the mixed noise removal, especially for the real and complex noise scenario of HSIs. Also, the proposed method maintains a higher model representation ability than traditional optimization-based methods.

The main contributions of this paper can be summarized as follows:

- 1) The DIP is well extended to fulfill the particular structure of HSIs by using the separable 3D convolutional blocks. Thus, it is possible to remove the mixed noise under the unsupervised condition with few network parameters and high model representation abilities brought from the separable 3D CNN.
- 2) A spatial-spectral total variation term, which fully explores the HSI spatial-spectral piecewise-smooth prior so that high-quality spatial and spectral information recovery could be guaranteed, is tailored in the loss function of the proposed separable 3D DIP framework. Moreover, it addresses the semi-convergence, which always exists in the DIP framework.
- 3) Extensive experiments illustrate that the proposed method removes the mixed noise well in terms of numerical eval-

uation and visual quality, and it also has a significant generalization capability for different types of visual data.

The rest of the paper is organized as follows. In Sec. II, we introduce some related works. Sec. III gives the details of the proposed method. In Sec. IV, extensive experiments are reported. Sec. V presents deeper discussions of the proposed method. Finally, Sec. VI gives conclusions of this paper.

## II. RELATED WORK

### A. Model-Based Methods For HSI Denoising

The early HSI denoising methods are mainly model-based. Well-known methods such as TV [7]–[11], sparsity driven methods [12], [13], and BM4D [34] are conventional techniques. Dictionary learning-based methods are also utilized in hyperspectral denoising [35], [36]. Recently, the matrix/tensor low-rank approximation-based methods have been extensively studied for HSI restoration [14]–[20]. For instance, Zhang *et al.* [14] vectorized each band of the HSI as a column and unfolds them as a matrix, and then consider the low-rank property of the unfolded matrix. Wang *et al.* [16] utilized the tensor decomposition, which delivers the global tensor low-rank to establish a state-of-the-art model-based denoising method.

### B. CNN-based methods For HSI Denoising

In recent years, the CNN-based approaches for HSI denoising [28]–[32] have emerged and present state-of-the-art performance. For instance, Yuan *et al.* [30] employed the deep residual CNN to conduct HSI denoising. Dong *et al.* [28] utilized the deep 3D encoder-decoder network for HSI denoising. The core concept of these methods is to train a CNN with abundant pairs of training data  $\{\mathcal{Y}, \mathcal{X}\}$ , where  $\mathcal{Y}$  denotes the dataset of noisy images and  $\mathcal{X}$  denotes the dataset of corresponding clean images. The general optimization model of the training process is described as

$$\Theta^* = \underset{\Theta}{\operatorname{argmin}} \mathcal{L}(f_{\Theta}(\mathcal{Y}), \mathcal{X}), \quad (2)$$

where  $f_{\Theta}(\cdot)$  denotes a CNN with parameter  $\Theta$ , and  $\mathcal{L}$  is the loss function. After certain training epochs, the CNN is sufficient to handle the denoising of the noisy image  $\mathcal{Z}$ , whose noisy-free estimation can be obtained by  $f_{\Theta^*}(\mathcal{Z})$ .

### C. Deep Image Prior

Recently, Ulyanov *et al.* proposed an unsupervised deep learning-based image restoration technique, named deep image prior [33]. The DIP uses CNN to conduct image restoration without any training process. By targeting the degraded image as the network output with randomly generated network input, the CNN could remove the Gaussian noise from the degraded image with appropriate iteration steps. Afterward, Sidorov *et al.* extended DIP into hyperspectral image restoration [1] and showed that both 2D convolution and 3D convolution in CNN can get an intrinsic prior of the HSI.

Similar to the supervised approaches, the optimization process of DIP for HSI [1] restoration is formulated as

$$\Theta^* = \underset{\Theta}{\operatorname{argmin}} \frac{1}{N} \|f_{\Theta}(\mathcal{Z}) - \mathcal{Y}\|_{\ell_2}^2, \quad (3)$$

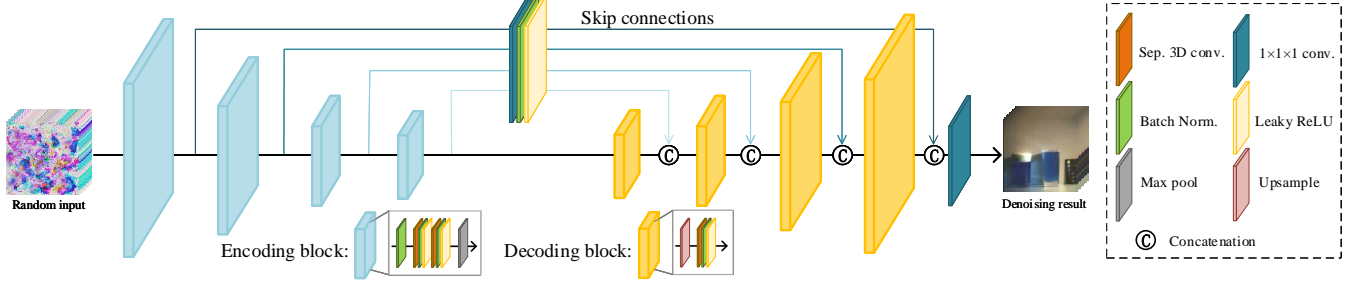


Fig. 2. The network structure of the proposed work. The separable 3D convolution-driven encoder-decoder network aims at preferably extracting the spatial and spectral features under the unsupervised condition.

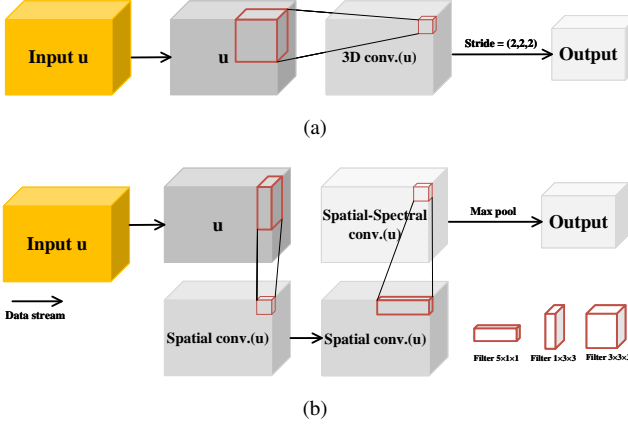


Fig. 3. Illustrations of (a) the traditional 3D convolutional block used in DIP [1], and (b) the proposed separable 3D convolutional block.

where  $\mathcal{Z} \in \mathbb{R}^{H \times W \times B}$  denotes the randomly generated network input.  $\mathcal{Y}$  is the to-be-reconstructed HSI. Here, mean square error (MSE) is adopted to present the loss function, where  $N = H \times W \times B$  denotes the number of total pixels. With randomly initialized network parameters, the optimization problem can be obtained using gradient descend method like ADAM [37]. Obviously, the optimization process will finally converge with a noisy image  $f_{\Theta^*}(\mathcal{Z})$ , which is almost structurally identical with the observation  $\mathcal{Y}$ . However, it has been discovered that the network will firstly fit the signal part of the observation, and then fit the noisy part [33]. Thus, the denoising of  $\mathcal{Y}$  can be achieved by stopping the iteration at appropriate steps before the network fitting noise.

### III. THE PROPOSED S2DIP

#### A. The Motivation

The hyperspectral mixed noise removal is a challenging task as the noise varies from different types and intensities. For the previous CNN-based approaches, some problems are existing in data acquisition: 1) it is difficult to obtain clean HSIs (much more difficult than 2D natural images). 2) when the sensor obtains the HSIs, the imaging condition is unsatisfactory, leading to extremely complex noise, which is difficult to model and parameterize. Thus, the supervised CNN-based methods suffer from inadequate generalizations.

In this paper, we propose to remove the mixed noise in HSIs in the unsupervised manner, based on DIP. However, the

current DIP framework has two undesirable factors for HSI mixed noise removal.

Firstly, directly extending 2D convolution-driven DIP to 3D convolution-driven DIP achieves limited effects [1]. In truth, the 3D convolution is expected to simultaneously represent the spatial and spectral features, while the spatial features and spectral features are not structurally consistent. Thus, the spatial and spectral features would be better exploited by different kernels. Meanwhile, the 3D convolution brings abundant network parameters, leading to high computational burdens.

In response to this issue, we employ the separable 3D convolution, inspired by its success in the supervised [28], [38] and self-supervised [39] fields. The separable 3D convolution uses 2D and 1D kernels to extract the spatial and spectral features respectively to fulfill the 3D structure of HSIs, while simultaneously reduces network parameters.

Another limitation of DIP is the semi-convergence. In truth, the DIP framework lacks extra guidances and constraints on the unsupervised learning process, which leads to weak ability in complex noise removal and causes semi-convergence.

To address the above issues, we attempt hand-crafted priors to constrain the DIP. With the 3D structure of HSIs, a spatial-spectral total variation term, which considers the spatial-spectral piecewise-smoothness, is meticulously selected as a regularization term in the loss function so that the high-quality spatial-spectral information recovery can be ensured.

The proposed S2DIP does not need any training data and maintains a high model representation ability with fewer network parameters, attributes to the well-designed separable 3D CNN. In the meantime, the SSTV loss brings significant progress in denoising abilities and alleviates the semi-convergence.

#### B. Separable 3D Convolutional Encoder-Decoder Network

For a three-way tensor of size  $H \times W \times B$ , a 3D kernel of size  $n \times n \times k$  (mostly  $3 \times 3 \times 3$ ) can be utilized to exploit both the spatial and spectral information of the HSI by striding 3 directions in sequence.

Unlike the 3D convolution, the separable 3D convolution extracts the spatial and spectral features by using 2D and 1D kernels respectively to commendably fulfill the unique structure of 3D HSIs. Specifically, the separable 3D convolution decomposes the 3D kernel of size  $3 \times 3 \times 3$  into two kernels of size  $3 \times 3 \times 1$  and  $1 \times 1 \times 5$ . The two kernels in a separable

3D convolutional block, which contains fewer convolutional parameters than a traditional 3D convolutional block, do three-dimensional convolution successively to extract spatial features and spectral features respectively (Fig. 3(b)).

An encoder-decoder network is employed for HSI denoising, seen in Fig. 2. With the separable 3D convolution and max pooling, the input data goes through the encoding stage and progressively outcomes embedded spatial-spectral features, which afterward goes through the decoding stage to reconstruct the clean HSI. Here, the number of convolutional layers in the encoding block is double that of the decoding block to favourably encode the data. Meanwhile, skip connections between the encoder and decoder are employed.

### C. SSTV Constrained DIP

Generally, the TV model maintains a powerful capability to characterize the smooth prior of natural images. In particular, for a three-way tensor  $\mathcal{X} \in \mathbb{R}^{H \times W \times B}$ , its difference tensors  $\mathbf{D}_v \mathcal{X} \in \mathbb{R}^{(H-1) \times W \times B}$ ,  $\mathbf{D}_h \mathcal{X} \in \mathbb{R}^{H \times (W-1) \times B}$ , and  $\mathbf{D}_b \mathcal{X} \in \mathbb{R}^{H \times W \times (B-1)}$  are determined by

$$\begin{cases} \mathbf{D}_v \mathcal{X}(i, j, k) = \mathcal{X}(i+1, j, k) - \mathcal{X}(i, j, k), \\ \mathbf{D}_h \mathcal{X}(i, j, k) = \mathcal{X}(i, j+1, k) - \mathcal{X}(i, j, k), \\ \mathbf{D}_b \mathcal{X}(i, j, k) = \mathcal{X}(i, j, k+1) - \mathcal{X}(i, j, k), \end{cases} \quad (4)$$

where  $\mathcal{X}(i, j, k)$  denotes the  $(i, j, k)$ -th element of  $\mathcal{X}$ , and  $\mathbf{D}_v$ ,  $\mathbf{D}_h$ , and  $\mathbf{D}_b$  denote the finite difference operators of the vertical direction, horizontal direction, and spectral direction, respectively. The TV of  $\mathcal{X}$  is given by

$$\mathbf{TV}(\mathcal{X}) = \|\mathbf{D}_v \mathcal{X}\|_{\ell_1} + \|\mathbf{D}_h \mathcal{X}\|_{\ell_1}. \quad (5)$$

Further, considering the spatial-spectral piecewise-smoothness, the spatial-spectral total variation (SSTV) [9] of  $\mathcal{X}$  is written as

$$\mathbf{SSTV}(\mathcal{X}) = \|\mathbf{D}_v(\mathbf{D}_b \mathcal{X})\|_{\ell_1} + \|\mathbf{D}_h(\mathbf{D}_b \mathcal{X})\|_{\ell_1}. \quad (6)$$

As a matter of fact, TV and SSTV are functionally complementary to each other, where TV considers the spatial local smoothness and SSTV delivers the spatial-spectral local smoothness. To faithfully utilize both of their properties, we introduce both TV and SSTV in the loss function to explore the spatial and spatial-spectral local smooth prior of HSIs under unsupervised conditions. By rewritten Eq. (3), the proposed optimization model can be described as

$$\boldsymbol{\Theta}^* = \underset{\boldsymbol{\Theta}}{\operatorname{argmin}} \left\{ \frac{1}{N} \|f_{\boldsymbol{\Theta}}(\mathcal{Z}) - \mathcal{Y}\|_{\ell_2}^2 + \lambda \mathbf{SSTV}_h(f_{\boldsymbol{\Theta}}(\mathcal{Z})) \right\}, \quad (7)$$

where

$$\mathbf{SSTV}_h(\cdot) = \alpha_1 \mathbf{TV}(\cdot) + \alpha_2 \mathbf{SSTV}(\cdot), \quad (8)$$

and  $\lambda$  is the hyperparameter that needs to be regulated.  $\alpha_1$  and  $\alpha_2$  are the parameters in the  $\mathbf{SSTV}_h$  term that balance the direct spatial piecewise-smoothness and spatial-spectral piecewise-smoothness.

The setting of  $\alpha_1$  and  $\alpha_2$  is essential to the proposed framework. We attempt different values and empirically set  $\alpha_2 = 1$  and  $\alpha_1 = 0.01$ , which preferably balances the spatial and spatial-spectral local smoothness, i.e., emphasizes more

on the spatial-spectral local smoothness and avoids the spatial over-smoothness.

### D. The Automatic Stopping Criterion

As DIP needs the ground-truth (GT) or manual stop on the iteration to ensure the quality of denoising results, in this paper, we introduce an automatic stopping criterion based on relative error

$$\text{RelErr} = \frac{\|\mathcal{O}_{k+1} - \mathcal{O}_k\|_{\ell_2}}{\|\mathcal{O}_k\|_{\ell_2}} \quad (9)$$

and iteration step. Here,  $\mathcal{O}_k \in \mathbb{R}^{H \times W \times B}$  denotes the  $k$ -th network output. Specifically, we set parameters  $r$  and  $k_{max}$  as the tolerance of **RelErr** and the maximum number of iteration steps, respectively. The iteration will be terminated if: 1) **RelErr** of the  $k$ -th iteration is lower than  $r$ , or 2) the iteration number  $k$  exceeds  $k_{max}$ . Cooperatively, **RelErr** evaluates the convergent degree of the optimization process while  $k_{max}$  guarantees the final stopping of the iteration.

## IV. EXPERIMENTS

Both simulation experiments and real data experiments are involved to verify the validity of the proposed method. Here, the competing methods are LRMR [14], LRTDTV [16], DIP based on 2D convolution (DIP 2D) and DIP based on traditional 3D convolution (DIP 3D) [1].

The hyperparameters of each method are set carefully. For LRMR, the parameters recommended by the authors are used. For LRTDTV, except for the parameters already recommended by authors, we test every case with different parameters setting, and to the best of our knowledge find the most promising results in terms of PSNR values (simulation experiments) and visual effects (real noise removal). For DIP and the proposed S2DIP, we set the learning rate as 0.005 to prevent gradient explosions that are occasionally happened during our testing.

Two programming languages including Python (DIP, S2DIP) and MATLAB (LRMR, LRTDTV) are needed to implement these methods. For fairness, all measurements are conducted in MATLAB, where *.npy* files, which contain the denoising results of DIP and the proposed method, are transformed into *.mat* files without any compression.

### A. Simulation Experiments

For simulation experiments, commonly adopted HSIs *Washington DC mall (WDC mall)* of size  $256 \times 256 \times 191$ , *Pavia centre* of size  $200 \times 200 \times 80$  and *Indian pines* of size  $145 \times 145 \times 224$  are involved to generate synthetic noisy images, where all HSIs are selected with 32 bands, i.e., from band 1 to band 32. Additionally, multispectral images (MSIs) in CAVE [40] dataset of size  $256 \times 256 \times 31$  with all spectral bands are adopted. The pixel values of images are normalized to the range  $[0, 1]$  band-to-band. In the meantime, 5 different noise levels are established, as can be seen in Table I. Based on the settings in Table I, all noises are generated randomly.

The denoising results are numerically evaluated by peak signal-to-noise ratio (PSNR), structure similarity (SSIM), and spectral angle mapper (SAM) [41]. Conventionally, larger

TABLE I

DATA USED IN EXPERIMENTS AND THE NOISE SETTING IN SIMULATION EXPERIMENTS.  $\sigma$  DENOTES THE STANDARD DEVIATION OF THE GAUSSIAN NOISE.  $p$  REFERS TO THE SAMPLING RATE OF THE IMPULSE NOISE.  $s_1$  AND  $s_2$  DENOTE THE NUMBERS OF STRIPES AND DEADLINES IN EACH CORRUPTED BAND, RESPECTIVELY.

Synthetic data: WDC mall, Pavia centre, Indian pines, CAVE [40] dataset.									
Noise setting	Cases	Gaussian noise		Impulse noise		Stripe		Deadline	
		added band	$\sigma$	added band	$p$	added band	$s_1$	added band	$s_2$
Noise setting	Case 1	all bands	0.2	--	--	--	--	--	--
	Case 2	all bands	0.1	all bands	0.1	--	--	--	--
	Case 3	all bands	0.1	all bands	0.1	40%	[6, 15]	--	--
	Case 4	all bands	0.1	all bands	0.1	--	--	50%	[6, 10]
	Case 5	all bands	0.1	all bands	0.1	40%	[6, 15]	50%	[6, 10]

Real data: Urban, Indian

TABLE II

THE METRICS OF THE DENOISING RESULTS BY DIFFERENT METHODS. (THE **best** VALUES ARE HIGHLIGHTED BY **boldface**. THE second-best VALUES ARE HIGHLIGHTED BY underline.)

Data		WDC mall			Pavia centre			Indian pines			CAVE		
Case	Methods	PSNR	SSIM	SAM	PSNR	SSIM	SAM	PSNR	SSIM	SAM	PSNR	SSIM	SAM
Case 1	LRMR [14]	24.368	0.555	0.635	24.235	0.562	0.311	23.766	0.546	0.161	24.258	0.346	0.770
	LRTDTV [16]	30.648	<u>0.813</u>	0.218	30.452	0.819	0.103	31.968	<u>0.905</u>	0.0505	32.372	0.852	0.351
	DIP 2D [1]	27.797	0.693	0.265	27.833	0.731	0.118	27.110	0.786	0.0887	31.375	0.792	0.237
	DIP 3D [1]	27.753	0.699	0.264	27.774	0.725	0.141	26.971	0.761	0.0925	31.169	0.763	0.286
	S2DIP	<u>30.965</u>	<b>0.843</b>	<u>0.199</u>	<u>31.030</u>	<u>0.853</u>	<u>0.0970</u>	<u>32.285</u>	<b>0.933</b>	<u>0.0471</u>	<u>35.297</u>	<u>0.924</u>	<u>0.140</u>
	S2DIP*	<b>31.088</b>	<b>0.843</b>	<b>0.188</b>	<b>31.154</b>	<b>0.855</b>	<b>0.0886</b>	<b>32.407</b>	<b>0.933</b>	<b>0.0464</b>	<b>35.478</b>	<b>0.930</b>	<b>0.125</b>
Case 2	LRMR	22.160	0.488	0.435	22.787	0.527	0.246	23.412	0.545	0.142	22.008	0.307	0.619
	LRTDTV	25.657	0.695	0.203	26.794	0.768	0.0914	28.829	0.866	0.0605	25.577	0.603	0.455
	DIP 2D	24.620	0.580	0.172	25.472	0.680	0.112	26.193	0.779	0.0788	25.884	0.601	0.373
	DIP 3D	24.713	0.615	0.210	25.844	0.703	0.111	26.333	0.765	0.0761	25.917	0.605	0.369
	S2DIP	<u>26.090</u>	<u>0.746</u>	<u>0.139</u>	<u>27.531</u>	<u>0.840</u>	<u>0.0574</u>	<u>29.752</u>	<u>0.921</u>	<u>0.0528</u>	<u>26.502</u>	<u>0.662</u>	<u>0.342</u>
	S2DIP*	<b>26.176</b>	<b>0.749</b>	<b>0.137</b>	<b>27.788</b>	<b>0.844</b>	<b>0.0573</b>	<b>30.280</b>	<b>0.922</b>	<b>0.0518</b>	<b>26.691</b>	<b>0.666</b>	<b>0.341</b>
Case 3	LRMR	21.290	0.464	0.454	21.926	0.503	0.265	22.927	0.536	0.149	21.210	0.294	0.632
	LRTDTV	24.280	0.671	0.253	25.351	0.741	0.113	27.691	0.851	0.0718	24.131	0.582	0.486
	DIP 2D	22.752	0.474	0.240	23.797	0.587	0.124	24.699	0.717	0.122	24.288	0.565	0.423
	DIP 3D	23.306	0.545	0.244	24.239	0.649	0.109	25.356	0.743	0.0895	24.435	0.566	0.402
	S2DIP	<u>24.421</u>	<u>0.655</u>	<u>0.159</u>	<u>25.617</u>	<u>0.783</u>	<u>0.0724</u>	<u>28.236</u>	<u>0.911</u>	<u>0.0547</u>	<u>24.984</u>	<b>0.622</b>	<u>0.381</u>
	S2DIP*	<b>24.459</b>	<b>0.656</b>	<b>0.155</b>	<b>25.690</b>	<b>0.784</b>	<b>0.0716</b>	<b>28.503</b>	<b>0.912</b>	<b>0.0532</b>	<b>25.060</b>	<u>0.621</u>	<b>0.379</b>
Case 4	LRMR	22.335	0.489	0.449	22.866	0.520	0.266	20.700	0.498	0.213	21.825	0.309	0.632
	LRTDTV	26.024	0.690	0.208	<u>27.327</u>	0.752	0.110	24.661	<u>0.784</u>	0.110	25.571	0.599	0.456
	DIP 2D	24.588	0.595	0.202	25.480	0.685	<u>0.0988</u>	25.886	0.766	0.0772	25.840	0.598	0.378
	DIP 3D	24.553	0.591	0.199	25.571	0.684	0.106	26.159	0.779	0.0695	25.903	0.606	0.369
	S2DIP	<u>26.080</u>	<u>0.746</u>	<u>0.145</u>	27.320	<b>0.823</b>	<b>0.0607</b>	<u>29.280</u>	<b>0.912</b>	<u>0.0501</u>	<u>26.534</u>	<u>0.664</u>	<u>0.342</u>
	S2DIP*	<b>26.153</b>	<b>0.747</b>	<b>0.143</b>	<b>27.555</b>	<u>0.822</u>	<b>0.0607</b>	<b>29.573</b>	<b>0.912</b>	<b>0.0463</b>	<b>26.716</b>	<b>0.666</b>	<b>0.341</b>
Case 5	LRMR	21.422	0.463	0.466	22.026	0.491	0.287	20.705	0.494	0.210	21.032	0.295	0.647
	LRTDTV	24.534	0.654	0.269	<u>25.917</u>	<u>0.708</u>	0.118	24.811	<u>0.784</u>	0.110	24.210	0.579	0.486
	DIP 2D	22.607	0.439	<u>0.221</u>	23.738	0.587	0.128	24.433	0.714	0.112	24.234	0.567	0.422
	DIP 3D	23.116	0.522	0.225	24.277	0.653	0.122	25.150	0.751	0.0903	24.413	0.568	0.404
	S2DIP	<u>24.540</u>	<b>0.677</b>	<b>0.149</b>	25.782	<b>0.802</b>	<b>0.0745</b>	<u>27.746</u>	<b>0.899</b>	<u>0.0563</u>	<u>24.886</u>	<u>0.618</u>	<u>0.381</u>
	S2DIP*	<b>24.545</b>	<u>0.671</u>	<b>0.149</b>	<b>25.995</b>	<b>0.802</b>	<u>0.0748</u>	<b>27.946</b>	<b>0.899</b>	<b>0.0553</b>	<b>25.010</b>	<b>0.620</b>	<b>0.378</b>

values of PSNR and SSIM represent higher qualities. However, SAM, which determines the spectral similarity between two HSIs, tends to have lower values if the two HSIs share more similarity on spectral structures.

DIP 2D and DIP 3D are arranged with 7000 iteration steps. The results of the highest PSNR value among all iterations

are reported. For the proposed method, we use the stopping criterion to decide the stopping point of S2DIP, which avoids the need for the GT. Specifically, the tolerance of  $\text{RelErr } r$  is set as 0.01 and the maximum iteration number  $k_{max}$  is set as 7000. For the hyperparameter  $\lambda$ , the cases with the same noise level are set with the same values as  $\frac{0.2}{N}, \frac{0.4}{N}, \frac{1}{N}, \frac{0.4}{N}$ ,

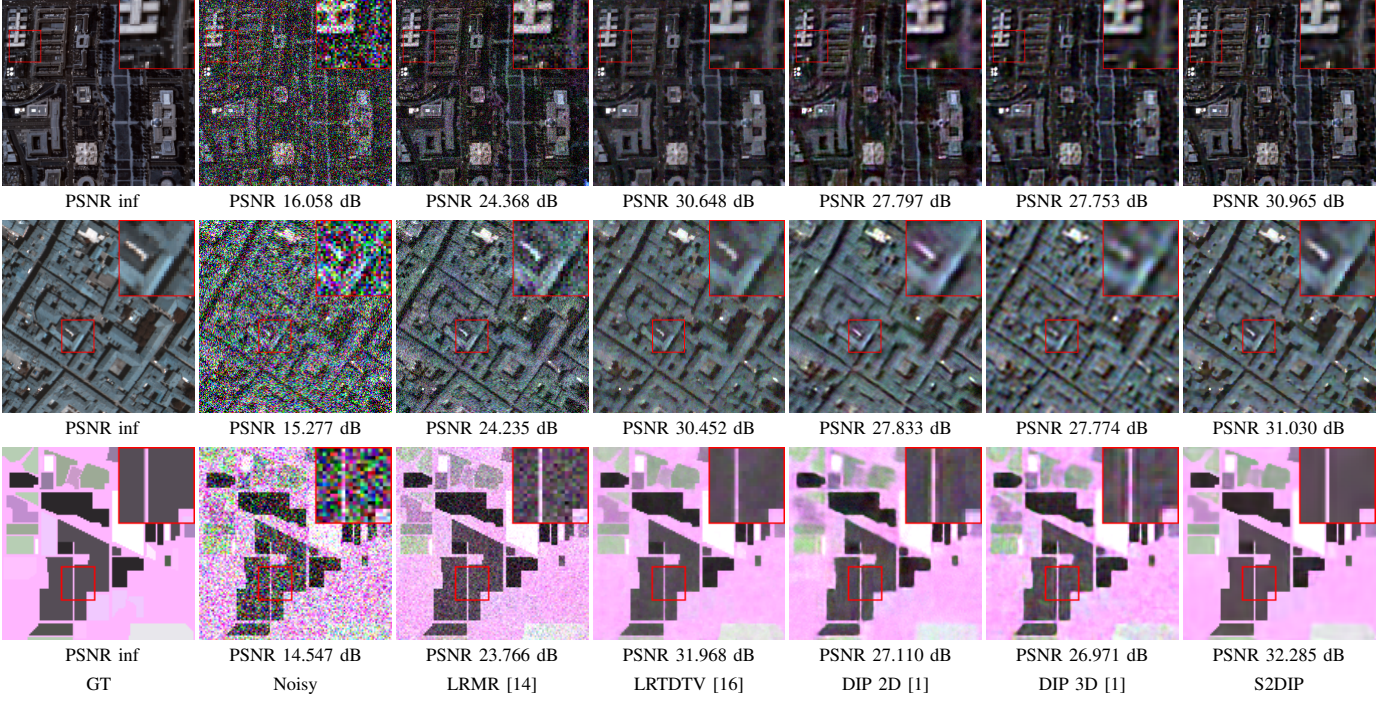


Fig. 4. The denoising hyperspectral images by different methods for the Case 1. Each row from top to down lists *WDC mall* consisted of the 14th, 15th, and 19th bands, *Pavia centre* consisted of the 10th, 20th, and 30th bands, and *Indian pines* consisted of the 15th, 25th, and 29th bands.

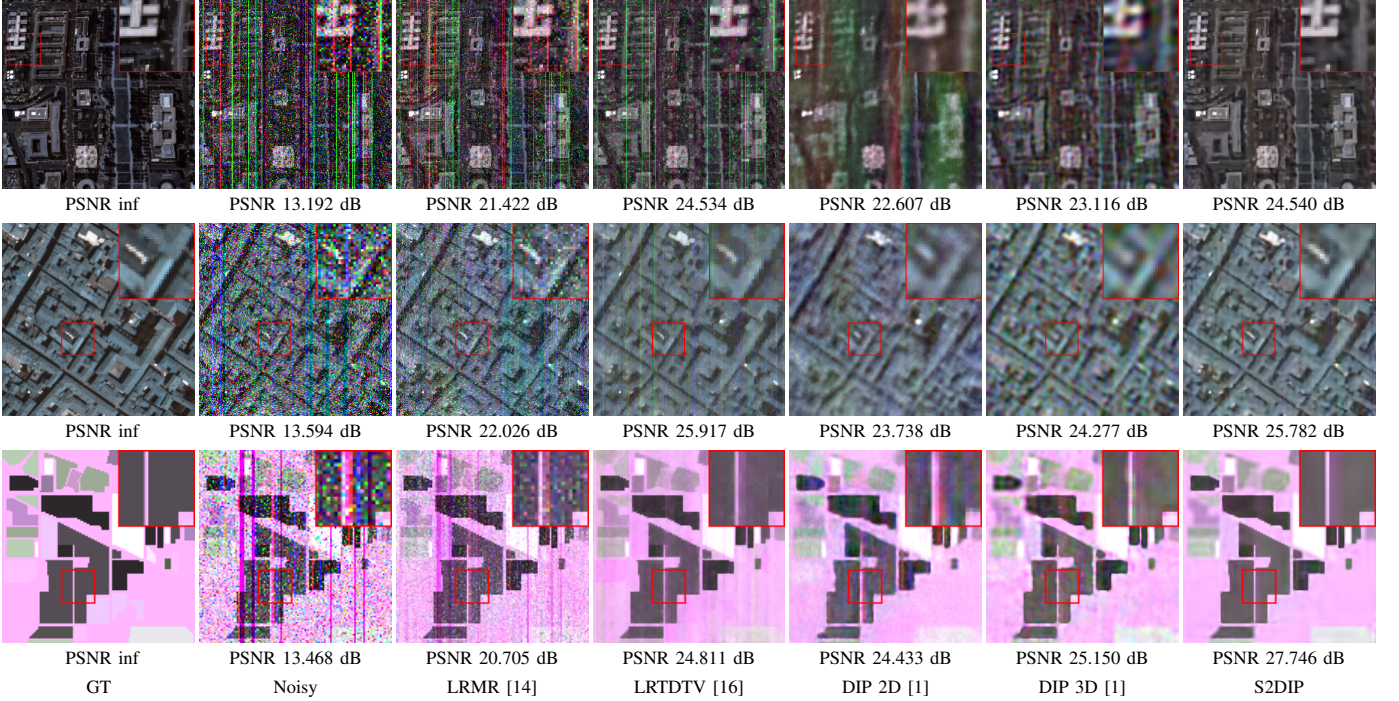


Fig. 5. The denoising hyperspectral images by different methods for the Case 5. Each row from top to down lists *WDC mall* consisted of the 7th, 17th, and 27th bands, *Pavia centre* consisted of the 10th, 20th, and 30th bands, and *Indian pines* consisted of the 15th, 25th, and 29th bands.

$\frac{1}{N}$  for Case 1-5 respectively, where  $N$  denotes the number of total pixels. In the following pages, we use “S2DIP” to denote the stopping criterion-based approach, and “S2DIP\*” denotes the best PSNR value among all iterations.

The numerical results are illustrated in Table II. The metrics of the CAVE dataset are calculated by averaging the results

of all 32 MSIs. One can discover that S2DIP\* outperforms competing methods for all cases, in terms of PSNR. The proposed method based on the stopping criterion (S2DIP) is also competitive between chosen methods, with PSNR index a little lower than “S2DIP\*” by 0.1-0.5 dB, which shows that S2DIP has convergence property to stably handle the mixed

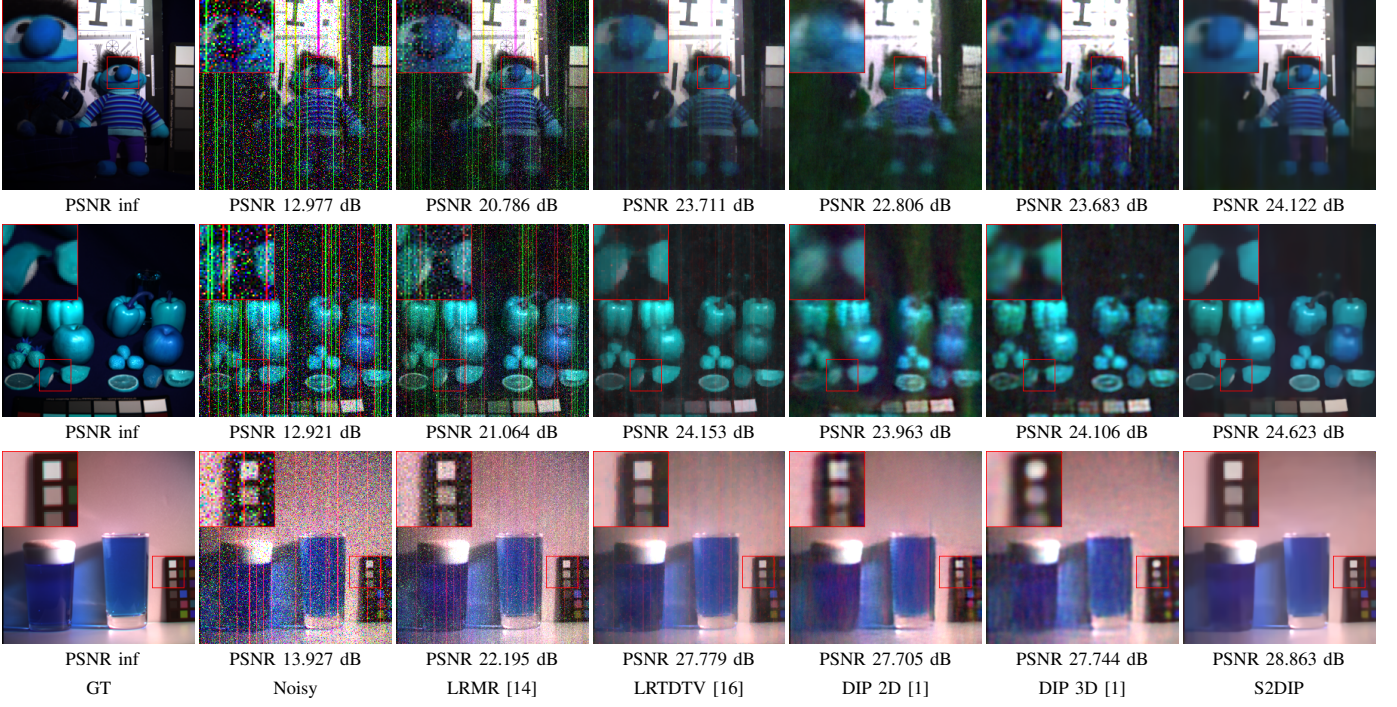


Fig. 6. The denoising multispectral images by different methods for the Case 5. Each row from top to down lists *Toy* images consisted of the 10th, 20th, and 30th bands, *Foods* images consisted of the 7th, 25th, and 30th bands, and *Cups* images consisted of the 1st, 10th, and 20th bands.

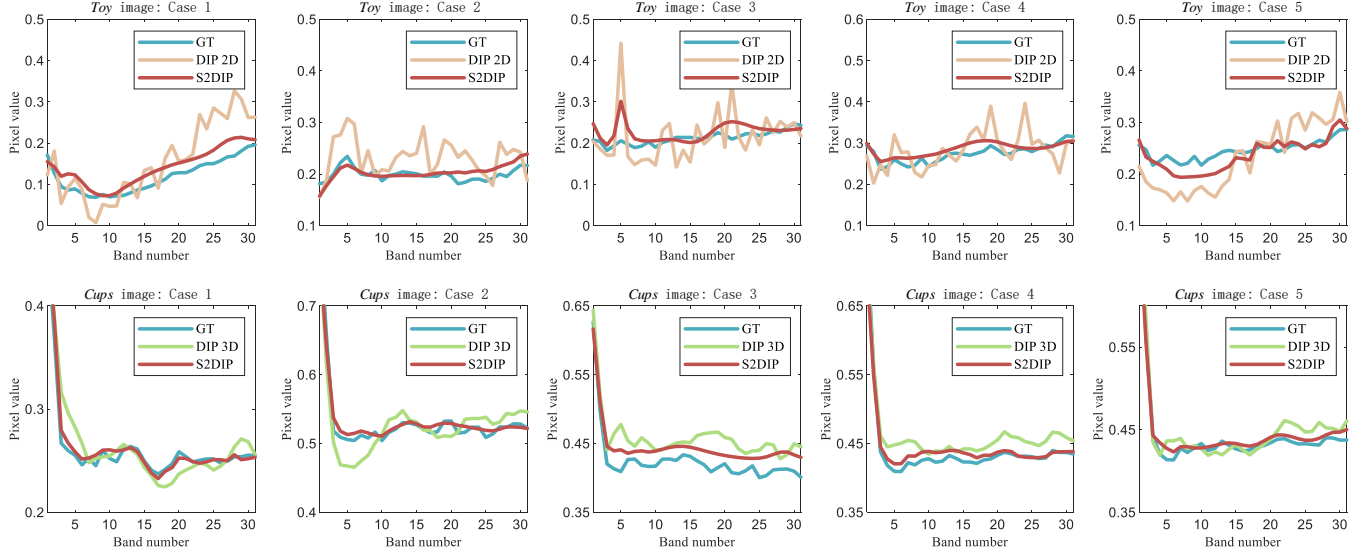


Fig. 7. Spectral curves of the selected pixels of clean images and denoising results on multispectral images *Toy* and *Cups* for Case 1-5.

noise removal under unsupervised conditions.

One limitation of DIP is the semi-convergence. In contrast, S2DIP is able to automatically deliver well-denoised images without any supervision. On the other hand, it proves that the stopping criterion is well-designed and gives an effective reference on the stopping point of the iteration.

It is notable that the SAM values of the proposed method are superior to competing methods. This mainly attributes to the spatial-spectral constraint of the proposed framework, where high-quality spatial-spectral correlation reinforcements are founded. In other words, the hand-crafted prior knowledge

is considered comprehensively and cooperates faithfully with the deep priors to enhance the quality of spatial and spectral recovery, leading to complete removal of the noise. Thus, the denoising results of the proposed method display more spectral similarity with GT images, *i.e.*, have lower SAM values.

In Fig. 4, the denoising results for the Case 1 (Gaussian noise only) are displayed. For this relatively low-level noise, we see that LRTDTV and S2DIP can both handle it well visually, while S2DIP achieves better PSNR values. We subsequently illustrate some denoising results for the Case 5 (Fig. 5), as it contains the most complex noise. For *WDC mall*,

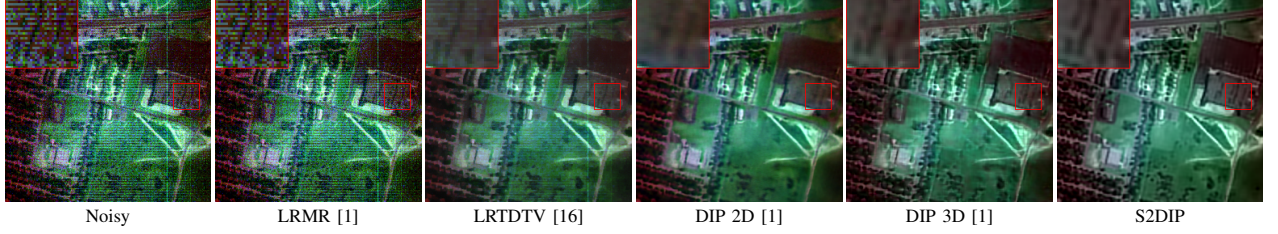


Fig. 8. The denoising hyperspectral images by different methods for *Urban* (The pesudo images consisted of the 139th, 150th, and 151th bands).

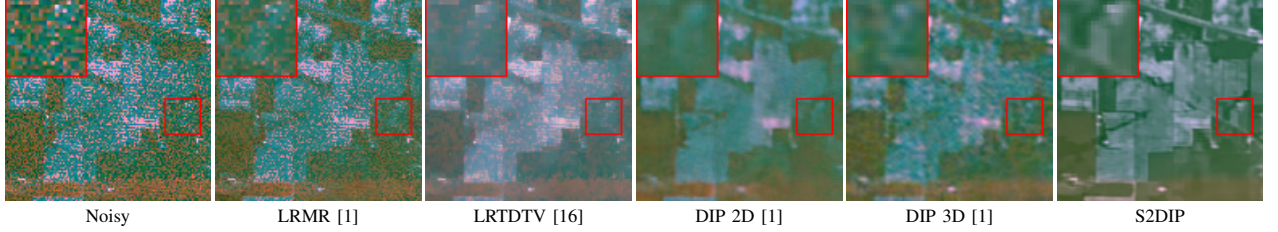


Fig. 9. The denoising hyperspectral images by different methods for *Indian* (The pesudo images consisted of the 1st, 2nd, and 3rd bands).

S2DIP manages to remove the complex noise and retains image features to some degree. In contrast, LRMR, which delivers the low-rankness by matrix, is hardly to recover the HSI. LRTDTV considers the global tensor low-rank, thus it achieves noise removal in partial bands, but fails to totally remove the stripes and impulses. Besides, DIP methods find difficulties fitting the signal part of the observation before fitting the complex noise, resulting in the inability to handle the removal of the complex noise. This phenomenon shows that the DIP framework lacks extra guidances and constraints on the unsupervised learning system, which causes weakness in denoising ability. For *Pavia centre*, S2DIP accomplishes the mixed noise removal while at the same time retains some obvious edges and image details, while DIP 2D and DIP 3D both miss image details in the zoom-in area. Again, DIP itself can hardly find a balance between fitting these details and avoiding fitting complex noise. For *Indian pines*, the proposed method could reconstruct the corrupted HSI and to a great extent retain the image edges, while competing methods couldn't remove the color distortion, according to the zoom-in figures.

Fig. 6 show some denoising results on *toy*, *foods*, and *cups* images that are selected from the CAVE dataset. For the *toy* image, LRTDTV and S2DIP both achieve good performance on recovering image details, while S2DIP has a better PSNR value. For the *foods* image, S2DIP successfully removes the complex noise while preserving image details. For the *cups* image, the color distortion is well-eliminated and the image structure is significantly recovered by S2DIP, which outperforms competing methods, according to the zoom-in figures.

In Fig. 7, we show the spectral curves of the selected pixels of the denoising results by DIP 2D, DIP 3D, and S2DIP. The less oscillating spectral curves of the denoising results by S2DIP verify that the spectral fidelity is well-preserved, compared with those of DIP 2D and DIP 3D. Collectively, the integration of the separable 3D CNN, which favorably exploits

spatial-spectral features, and the spatial-spectral constraint by the SSTV loss contributes to this phenomenon.

### B. Real Experiments

In this section, real noisy images *Urban* of size  $307 \times 307 \times 210$  with its band 134 to band 165 and *Indian* of size  $145 \times 145 \times 220$  with its band 1 to band 32 are included for the testing of real noise removal. As the GT is not available for real data, the results of DIP 2D and DIP 3D are manually chosen for their best performance. And the denoised quality is visually evaluated. The proposed method continues to use the stopping criterion, where  $r$ ,  $k_{max}$ , and  $\lambda$  is set as 0.01, 7000, and  $\frac{1}{N}$ , respectively.

The denoising results for *Urban* are displayed in Fig. 8, where S2DIP shows great performance to remove the complex noise. DIP 3D and DIP 2D also accomplish decent results but miss some image details, according to the zoom-in figures. These image details, which only appear in adjacent bands, are not likely to be exploited by 2D convolution where 2D kernels can only capture spatial information. For 3D convolution, although it can obtain some of these details, it ignores the spectral consistency by directly sums up spatial and spectral features. In contrast, the proposed method employs the separable 3D convolution to not only remove the complex noise but commendably utilize the spatial-spectral information from band-to-band.

The denoising results for *Indian* are illustrated in Fig. 9. The displayed spectral bands contain strong noise, and the first band is significantly corrupted. So the restorations of these bands are with great difficulties. As can be seen, LRTDTV and DIP 2D both remove the strong noise but LRTDTV produces color distortion while DIP 2D suffers from over-smoothness. In contrast, the proposed S2DIP successfully and reasonably restores the spatial-spectral structure of the corrupted images, showing outstanding performance compared with the competing methods.

TABLE III  
THE AVERAGE METRICS OF THE DENOISING RESULTS BY DIP 2D [1], DIP 3D [1], AND DIP S3D.

Cases	Method	Parameters	PSNR	SSIM	SAM
CAVE Case 1	DIP 2D	2.1M	<u>31.375</u>	<u>0.792</u>	<b>0.237</b>
	DIP 3D	1.6M	31.169	0.763	0.309
	DIP S3D	0.8M	<b>31.851</b>	<b>0.836</b>	<u>0.241</u>

For real experiments, the stopping criterion takes full advantage of the stable convergence of S2DIP, thus it is possible to remove the mixed noise without manual selections. In contrast, DIP 2D and DIP 3D still need manual selections to ensure the denoising quality. Therefore, S2DIP maintains a higher practical application value.

## V. DISCUSSION

### A. Effectiveness of SSTV Loss

In this subsection, we discuss the effectiveness of the SSTV loss from two aspects. Firstly, the SSTV loss improves the performance of the original DIP, in terms of the denoising ability and stability. Specifically, the TV and SSTV in the loss function provide spatial-spectral constraints so that the spatial-spectral fidelity enhancement in higher qualities can be ensured. Also, the SSTV loss determines the convergence property of the proposed method to ensure the quality of the auto-selected output image, which alleviates the semi-convergence of DIP.

Secondly, we illustrate that employing SSTV in the loss function improves the performance of the direct implementation of SSTV in traditional minimization problems. Here, we consider the hybrid spatial-spectral total variation (HSSTV) model [10] as another competing method. Generally, the difference between HSSTV and the proposed method is that we introduce TV and SSTV in the loss function while HSSTV employs TV and SSTV regularizers in a traditional minimization problem. Here, we attempt different parameter settings and obtain the best denoising results by HSSTV on CAVE dataset for the Case 5, in terms of PSNR values.

The average metrics of the 32 denoising MSIs by HSSTV is 21.404 for PSNR, 0.441 for SSIM, and 0.482 for SAM. In contrast, S2DIP achieves 24.886 for PSNR, 0.618 for SSIM, and 0.381 for SAM, which considerably outperforms HSSTV. Generally, the great representation ability of CNN contributes to the high effectiveness of SSTV loss. Fig. 10 shows an example of the denoising results, where S2DIP achieves high qualities on ameliorating the visual effect of the corrupted MSI, while HSSTV can not completely remove the impulse noise and stripe.

Eventually, we demonstrate that the SSTV loss presents an efficient technique for integrating the deep learning and hand-crafted denoisers into a uniform framework, which takes advantages of both the “deep prior” of CNN and the traditional image priors, and leads to better performance against each one of them.

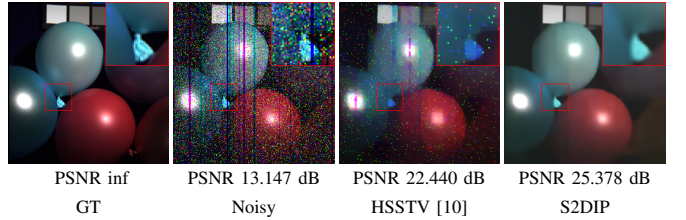


Fig. 10. The denoising multispectral images balloons (the pesudo images consisted of the 10th, 20th, and 30th bands) by different methods.

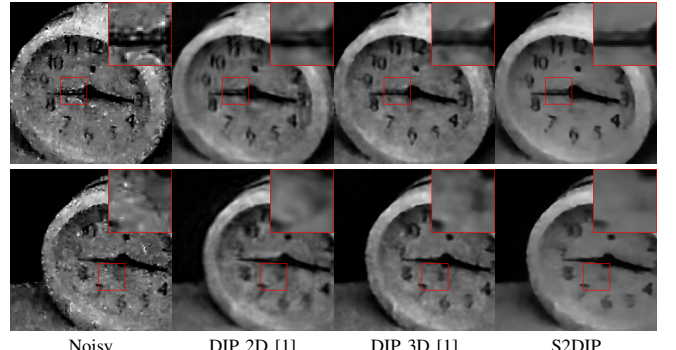


Fig. 11. Two denoising video frames by different methods.

### B. Effectiveness of Separable 3D Convolution

The separable 3D convolution in the CNN provides effective spatial and spectral features extraction to boost the performance of the proposed unsupervised framework. Meanwhile, the separable implementation of the 3D convolution reduces the parameters in a 3D convolutional block which helps to build a light-weight network.

To illustrate the effectiveness of separable 3D DIP, we test the proposed method without TV and SSTV in the loss function, *i.e.*, the proposed method recovers DIP that driven by separable 3D convolution. Here, the denoising results are selected by the highest PSNR value, and we consider Case 1 (Gaussian noise only) because of the inability of DIP to handle complex noise. The numerical results are displayed in Table III. Conclusively, DIP S3D, which denotes the separable 3D-driven DIP, outperforms DIP 3D in terms of network weights and numerical evaluations, and also shows competitiveness against DIP 2D whose network contains a large number of convolutional parameters.

Noting that the traditional 3D convolution also uses 3D filters to striding three directions to exploit spatial and spectral features simultaneously, however, as the HSI spatial and spectral components are structurally inconsistent, they would be better handled by different kernels [39], [42]. The proposed method uses separable 3D convolution, which employs two kernels to successively exploit the spatial and spectral information under the unsupervised condition, to provide efficient features extraction, while simultaneously reducing network parameters.

### C. The Generalization of S2DIP

In this subsection, we discuss the generalization of the proposed method. Here, we consider video data<sup>1</sup> which also contains three dimensional information. In low light conditions, the videos will be inevitably corrupted by dynamic noise [43], as seen in Fig. 11.

Owing to the complexity and irregularity of the real noise, the video denoising is extremely challenging. For the heavily corrupted video frames, we tentatively utilize DIP and our method for its restoration. Fig. 11 displays the denoising results, where S2DIP reasonably recovers the clean video and preserve the temporal fidelity, while the results of DIP methods, which are selected manually, remain notable noise. The aforementioned observations illustrate the generalization of S2DIP to handle different types of data except for HSIs and MSIs, e.g., video data.

In truth, the video data and HSIs are structurally homologous, as they both possess local smoothness in the spatial domain as well as the spatial-temporal/spectral domain. Hence, the SSTV in the loss function effectively constrains the learning process to faithfully handle the denoising of the video data.

## VI. CONCLUSION

In this paper, we propose the S2DIP for hyperspectral mixed noise removal. The separable 3D convolution is employed to preferably capture the spatial-spectral correlation with fewer parameters, and the DIP framework is combined with the SSTV loss to fully explore the HSI spatial-spectral local smooth prior. Experimental results on synthetic data and real data demonstrate the effectiveness of the proposed method, which could lead to properly reconstructed output, hence achieves high-quality denoising results. Moreover, the proposed method alleviates the semi-convergence, which always exists in the DIP framework. At last, the proposed method is provided with strong generalization ability, thus it can be used to deal with strong and mixed noise removal in different types of data.

## REFERENCES

- [1] O. Sidorov and J. Y. Hardeberg, “Deep hyperspectral prior: Single-image denoising, inpainting, super-resolution,” in *2019 IEEE/CVF International Conference on Computer Vision Workshop (ICCVW)*, 2019, pp. 3844–3851.
- [2] G. Wang, Y. Zhang, B. He, and K. T. Chong, “A framework of target detection in hyperspectral imagery based on blind source extraction,” *IEEE Journal of Selected Topics in Applied Earth Observations and Remote Sensing*, vol. 9, no. 2, pp. 835–844, 2016.
- [3] Y. Liu, G. Gao, and Y. Gu, “Tensor matched subspace detector for hyperspectral target detection,” *IEEE Transactions on Geoscience and Remote Sensing*, vol. 55, no. 4, pp. 1967–1974, 2017.
- [4] S. Jia, L. Shen, J. Zhu, and Q. Li, “A 3-D gabor phase-based coding and matching framework for hyperspectral imagery classification,” *IEEE Transactions on Cybernetics*, vol. 48, no. 4, pp. 1176–1188, 2018.
- [5] N. Akhtar and A. Mian, “Nonparametric coupled bayesian dictionary and classifier learning for hyperspectral classification,” *IEEE Transactions on Neural Networks and Learning Systems*, vol. 29, no. 9, pp. 4038–4050, 2018.
- [6] C. Liu, J. Li, L. He, A. Plaza, S. Li, and B. Li, “Naive gabor networks for hyperspectral image classification,” *IEEE Transactions on Neural Networks and Learning Systems*, pp. 1–15, 2020.
- [7] Q. Yuan, L. Zhang, and H. Shen, “Hyperspectral image denoising employing a spectral-spatial adaptive total variation model,” *IEEE Transactions on Geoscience and Remote Sensing*, vol. 50, no. 10, pp. 3660–3677, 2012.
- [8] W. He, H. Zhang, H. Shen, and L. Zhang, “Hyperspectral image denoising using local low-rank matrix recovery and global spatial-spectral total variation,” *IEEE Journal of Selected Topics in Applied Earth Observations and Remote Sensing*, vol. 11, no. 3, pp. 713–729, 2018.
- [9] H. K. Aggarwal and A. Majumdar, “Hyperspectral image denoising using spatio-spectral total variation,” *IEEE Geoscience and Remote Sensing Letters*, vol. 13, no. 3, pp. 442–446, 2016.
- [10] S. Takeyama, S. Ono, and I. Kumazawa, “Mixed noise removal for hyperspectral images using hybrid spatio-spectral total variation,” in *2019 IEEE International Conference on Image Processing (ICIP)*, 2019, pp. 3128–3132.
- [11] J. Liu, Y. Sun, X. Xu, and U. S. Kamilov, “Image restoration using total variation regularized deep image prior,” in *ICASSP 2019 - 2019 IEEE International Conference on Acoustics, Speech and Signal Processing (ICASSP)*, 2019, pp. 7715–7719.
- [12] J. Mairal, F. Bach, J. Ponce, G. Sapiro, and A. Zisserman, “Non-local sparse models for image restoration,” in *2009 IEEE 12th International Conference on Computer Vision*, 2009, pp. 2272–2279.
- [13] W. Dong, L. Zhang, G. Shi, and X. Li, “Nonlocally centralized sparse representation for image restoration,” *IEEE Transactions on Image Processing*, vol. 22, no. 4, pp. 1620–1630, 2013.
- [14] H. Zhang, W. He, L. Zhang, H. Shen, and Q. Yuan, “Hyperspectral image restoration using low-rank matrix recovery,” *IEEE Transactions on Geoscience and Remote Sensing*, vol. 52, no. 8, pp. 4729–4743, 2014.
- [15] W. He, H. Zhang, L. Zhang, and H. Shen, “Total-variation-regularized low-rank matrix factorization for hyperspectral image restoration,” *IEEE Transactions on Geoscience and Remote Sensing*, vol. 54, no. 1, pp. 178–188, 2016.
- [16] Y. Wang, J. Peng, Q. Zhao, Y. Leung, X. Zhao, and D. Meng, “Hyperspectral image restoration via total variation regularized low-rank tensor decomposition,” *IEEE Journal of Selected Topics in Applied Earth Observations and Remote Sensing*, vol. 11, no. 4, pp. 1227–1243, 2018.
- [17] Y. Chang, L. Yan, and S. Zhong, “Hyper-laplacian regularized unidirectional low-rank tensor recovery for multispectral image denoising,” in *2017 IEEE Conference on Computer Vision and Pattern Recognition (CVPR)*, 2017, pp. 5901–5909.
- [18] A. Karami, M. Yazdi, and A. Zolghadre Asli, “Noise reduction of hyperspectral images using kernel non-negative tucker decomposition,” *IEEE Journal of Selected Topics in Signal Processing*, vol. 5, no. 3, pp. 487–493, 2011.
- [19] Q. Xie, Q. Zhao, D. Meng, and Z. Xu, “Kronecker-basis-representation based tensor sparsity and its applications to tensor recovery,” *IEEE Transactions on Pattern Analysis and Machine Intelligence*, vol. 40, no. 8, pp. 1888–1902, 2018.
- [20] X. Chen, Z. Han, Y. Wang, Q. Zhao, D. Meng, L. Lin, and Y. Tang, “A generalized model for robust tensor factorization with noise modeling by mixture of gaussians,” *IEEE Transactions on Neural Networks and Learning Systems*, vol. 29, no. 11, pp. 5380–5393, 2018.
- [21] K. H. Jin, M. T. McCann, E. Froustey, and M. Unser, “Deep convolutional neural network for inverse problems in imaging,” *IEEE Transactions on Image Processing*, vol. 26, no. 9, pp. 4509–4522, 2017.
- [22] X. Mao, C. Shen, and Y.-B. Yang, “Image restoration using very deep convolutional encoder-decoder networks with symmetric skip connections,” in *Advances in Neural Information Processing Systems 29*, 2016, pp. 2802–2810.
- [23] K. He, X. Zhang, S. Ren, and J. Sun, “Deep residual learning for image recognition,” in *2016 IEEE Conference on Computer Vision and Pattern Recognition (CVPR)*, 2016, pp. 770–778.
- [24] Y. Tang, W. Gong, X. Chen, and W. Li, “Deep inception-residual laplacian pyramid networks for accurate single-image super-resolution,” *IEEE Transactions on Neural Networks and Learning Systems*, vol. 31, no. 5, pp. 1514–1528, 2020.
- [25] R. Dian, S. Li, A. Guo, and L. Fang, “Deep hyperspectral image sharpening,” *IEEE Transactions on Neural Networks and Learning Systems*, vol. 29, no. 11, pp. 5345–5355, 2018.
- [26] W. Xie, J. Lei, Y. Cui, Y. Li, and Q. Du, “Hyperspectral pansharpening with deep priors,” *IEEE Transactions on Neural Networks and Learning Systems*, vol. 31, no. 5, pp. 1529–1543, 2020.
- [27] P. Zhong and R. Wang, “Jointly learning the hybrid CRF and MLR model for simultaneous denoising and classification of hyperspectral

<sup>1</sup>The real noisy video is captured by a personal mobile phone under extremely low light condition.

imagery,” *IEEE Transactions on Neural Networks and Learning Systems*, vol. 25, no. 7, pp. 1319–1334, 2014.

[28] W. Dong, H. Wang, F. Wu, G. Shi, and X. Li, “Deep spatial–spectral representation learning for hyperspectral image denoising,” *IEEE Transactions on Computational Imaging*, vol. 5, no. 4, pp. 635–648, 2019.

[29] Y. Chang, L. Yan, H. Fang, S. Zhong, and W. Liao, “HSI-DeNet: Hyperspectral image restoration via convolutional neural network,” *IEEE Transactions on Geoscience and Remote Sensing*, vol. 57, no. 2, pp. 667–682, 2019.

[30] Q. Yuan, Q. Zhang, J. Li, H. Shen, and L. Zhang, “Hyperspectral image denoising employing a spatial–spectral deep residual convolutional neural network,” *IEEE Transactions on Geoscience and Remote Sensing*, vol. 57, no. 2, pp. 1205–1218, 2019.

[31] Y. Chang, M. Chen, L. Yan, X.-L. Zhao, Y. Li, and S. Zhong, “Toward universal stripe removal via wavelet-based deep convolutional neural network,” *IEEE Transactions on Geoscience and Remote Sensing*, vol. PP, pp. 1–18, 12 2019.

[32] K. Wei, Y. Fu, and H. Huang, “3-D quasi-recurrent neural network for hyperspectral image denoising,” *IEEE Transactions on Neural Networks and Learning Systems*, pp. 1–13, 2020.

[33] V. Lempitsky, A. Vedaldi, and D. Ulyanov, “Deep image prior,” in *2018 IEEE/CVF Conference on Computer Vision and Pattern Recognition*, 2018, pp. 9446–9454.

[34] M. Maggioni, V. Katkovnik, K. Egiazarian, and A. Foi, “Nonlocal transform-domain filter for volumetric data denoising and reconstruction,” *IEEE Transactions on Image Processing*, vol. 22, no. 1, pp. 119–133, 2013.

[35] M. Elad and M. Aharon, “Image denoising via sparse and redundant representations over learned dictionaries,” *IEEE Transactions on Image Processing*, vol. 15, no. 12, pp. 3736–3745, 2006.

[36] Y. Peng, D. Meng, Z. Xu, C. Gao, Y. Yang, and B. Zhang, “Decomposable nonlocal tensor dictionary learning for multispectral image denoising,” in *2014 IEEE Conference on Computer Vision and Pattern Recognition*, 2014, pp. 2949–2956.

[37] D. Kingma and J. Ba, “ADAM: A method for stochastic optimization,” *International Conference on Learning Representations*, 12 2014.

[38] Z. Qiu, T. Yao, and T. Mei, “Learning spatio-temporal representation with pseudo-3d residual networks,” in *2017 IEEE International Conference on Computer Vision (ICCV)*, 2017, pp. 5534–5542.

[39] R. Imamura, T. Itasaka, and M. Okuda, “Self-supervised hyperspectral image restoration using separable image prior,” *ArXiv*, vol. abs/1907.00651, 2019.

[40] F. Yasuma, T. Mitsunaga, D. Iso, and S. K. Nayar, “Generalized assorted pixel camera: Postcapture control of resolution, dynamic range, and spectrum,” *IEEE Transactions on Image Processing*, vol. 19, no. 9, pp. 2241–2253, 2010.

[41] B. R. Shivakumar and S. V. Rajashekharadhy, “Performance evaluation of spectral angle mapper and spectral correlation mapper classifiers over multiple remote sensor data,” in *2017 Second International Conference on Electrical, Computer and Communication Technologies (ICECCT)*, 2017, pp. 1–6.

[42] X. Ding, Y. Guo, G. Ding, and J. Han, “ACNet: Strengthening the kernel skeletons for powerful CNN via asymmetric convolution blocks,” in *2019 IEEE/CVF International Conference on Computer Vision (ICCV)*, 2019, pp. 1911–1920.

[43] W. Wang, X. Chen, C. Yang, X. Li, X. Hu, and T. Yue, “Enhancing low light videos by exploring high sensitivity camera noise,” in *2019 IEEE/CVF International Conference on Computer Vision (ICCV)*, 2019, pp. 4110–4118.